POLITECNICO
MILANO 1863

SCUOLA DI INGEGNERIA INDUSTRIALE
E DELL'INFORMAZIONE

Executive Summary of the Thesis

An Immersed Boundary method for fish-like swimming simulations

Laurea Magistrale in Mathematical Engineering - Ingegneria Matematica

Author: Cássio Murakami

Advisor: Prof. Nicola Parolini

Co-advisor: dr. Giorgio Negrini

Academic year: 2022-2023

1. Introduction

The exploration of fish-like swimming extends beyond its significance in biology, reaching into the realm of engineering applications. In the field of applied sciences, studying this phenomenon, shaped by millions of years of evolution, is essential for optimizing underwater propulsion systems and fine-tuning aerodynamic designs to elevate maneuverability performance. In the field of Computational Fluid Dynamics (CFD), numerous studies have explored the dynamics of fish-like swimming, with a specific emphasis on the scenario of fixed swimming. In this situation, the swimmer's body is fixed at a specific point within a uniform external flow, showcasing an undulating motion that embodies the essence of swimming. The objective is to examine thrust forces and vorticity patterns within the wake structure.
The objective of this study is to model the fish-like swimming scenario, simulate it using the *open-source* software OpenFOAM, which adopts the Finite Volume method (FVM), and analyze the characteristics of the obtained results. To account for the effects of the immersed body in the mathematical formulation, the study will employ the Immersed Boundary method (IBM) with a structured non-conforming mesh.

2. Mathematical Model

Modelling the fish-like swimming scenario involves deriving the governing partial differential equations, developing a numerical algorithm for solving the system, and describing the kinematics of the immersed body.

2.1. Fluid dynamics model

The project relies on assumptions of incompressibility, homogeneity, and Newtonian fluid behavior, with negligible temperature effects on fluid properties.
Consider the time $t \in [0, +\infty)$ and the spatial dimension d. Let $\Omega_f^t \subset \mathbb{R}^d$ denote the fluid domain, and Γ^t be the boundary of the structure. Let $\mathbf{u}$ denote the Eulerian velocity field, p the pressure field, $\mathbf{X}$ the structure Lagrangian map, ρ the fluid density, ν the kinematic viscosity, $\mathbf{f}$ the volume forces, and $\mathbf{f}_{\Gamma^t}$ the force exchange at the interface. The governing equations for the system consist of the incompressible Navier-Stokes equations coupled with the immersed boundary condition:

$$\begin{cases} \dfrac{\partial \mathbf{u}}{\partial t} + (\mathbf{u}\cdot\nabla)\mathbf{u} - \nu\Delta\mathbf{u} + \dfrac{1}{\rho}\nabla p = \mathbf{f} + \delta_{\Gamma^t}\mathbf{f}_{\Gamma^t}, \quad \text{in } \Omega_f^t,\ t>0 \\ \nabla\cdot\mathbf{u} = 0, \quad \text{in } \Omega_f^t,\ t>0 \\ \mathbf{u} = \dfrac{\mathrm{d}\mathbf{X}}{\mathrm{d}t}, \quad \text{in } \Gamma^t,\ t>0 \\ + \text{Boundary Conditions on } \partial\Omega_f^t/\Gamma^t \\ + \text{Initial Conditions} \end{cases}$$

where δ_{Γ^t} is the Dirac delta function with support on Γ^t.
Let $\mathbf{e}_x$ and $\mathbf{e}_y$ respectively denote the unit vectors parallel and orthogonal to the freestream, and $\mathrm{D}(\mathbf{u}) = \frac{1}{2}(\nabla\mathbf{u} + \nabla^T\mathbf{u})$. Consider F_D as the drag force and F_L as the lift force, defined as

$$\begin{aligned} F_D &= \oint_{\Gamma^t} (p\mathbf{n} - 2\mu\mathrm{D}(\mathbf{u})\mathbf{n}) \cdot \mathbf{e}_x \mathrm{d}S, \\ F_L &= \oint_{\Gamma^t} (p\mathbf{n} - 2\mu\mathrm{D}(\mathbf{u})\mathbf{n}) \cdot \mathbf{e}_y \mathrm{d}S. \end{aligned} \tag{1}$$

2.2. Immersed Boundary method

The FVM involves discretizing space into a computational tessellation of cells with finite volumes. This transformation converts the partial differential equation continuous problem into a set of algebraic expressions.
To integrate the IBM formulation into the problem, analyze Figure 1, which illustrates the boundary Σ of the discrete immersed surface and delineates the mesh into fluid cells, Immersed Boundary (IB) cells, and solid cells.

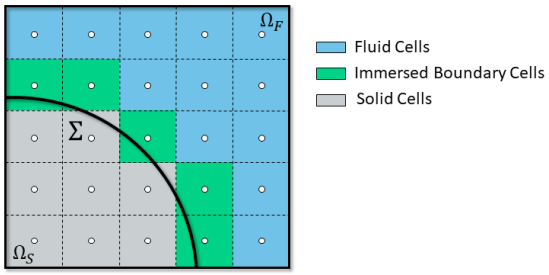

Figure 1: 2D representation of the mesh subdivision into solid cells $\mathcal{C}_\mathrm{S}$, fluid cells $\mathcal{C}_\mathrm{F}$, and IB cells $\mathcal{C}_\mathrm{IB}$.

The Immersed Boundary method involves creating an operator to correct the velocity field in the solid and IB cells. To evaluate the value of the IB cells, an interpolation of the extended stencil cells condition u_j and the projection into the surface condition $g_{\mathrm{IB},i}$ is performed:

$$\mathbf{U}^{\mathrm{corr}} = \begin{cases} s_{\mathrm{IB},i} g_{\mathrm{IB},i} + \sum\limits_{C_j \in \mathcal{S}_i} s_j u_j, & \text{if } C_i \in \mathcal{C}_\mathrm{IB} \\ g_i, & \text{if } C_i \in \mathcal{C}_\mathrm{S} \\ u_i, & \text{if } C_i \in \mathcal{C}_\mathrm{F} \end{cases}$$

In Figure 2, the scheme of the PIMPLE-IBM algorithm is presented, illustrating the approach employed to partition and solve the algebraic system. The PIMPLE-IBM algorithm is derived from the SIMPLE and PISO methods, incorporating the Immersed Boundary method corrections.

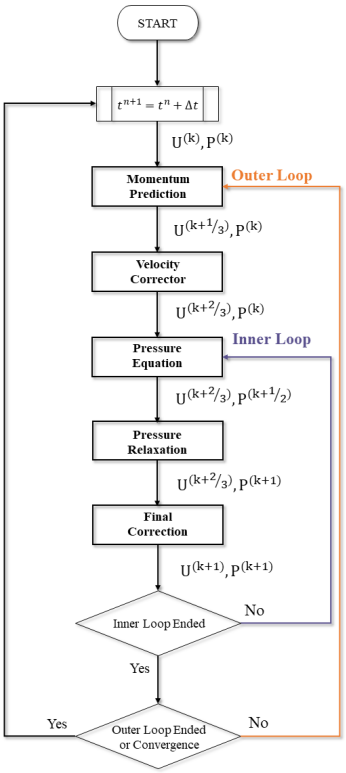

Figure 2: PIMPLE algorithm flowchart.

The IBM algorithm was implemented in the OpenFOAM software, building upon the work outlined in [4].

2.3. Fish-like swimming model

The geometry of the two-dimensional fish is constructed using the Karman-Trefftz conformal map. This mathematical transformation, parameterized to fit specific characteristics, morphs a circular shape into a configuration resembling an airfoil, as illustrated in the Figure 3.

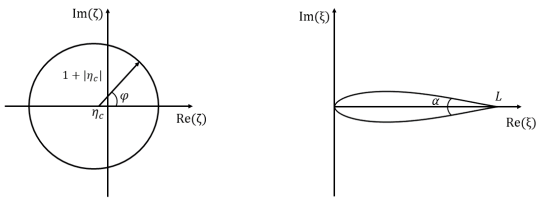

(a) Circle parametrization. (b) Airfoil parametrization.

Figure 3: Karman-Trefftz transform.

To prescribe the kinematics of the backbone of the fish, a backward travelling wave function $y(x,t)$ is employed. Let α represent the tail amplitude, $\mathrm{Tr}(t)$ the transient function, f the oscil-

lation frequency, λ the wavelength, and ϕ denote the phase of the wave, such that

$$y(x,t) = \alpha \mathrm{Tr}(t) A_m(x) \sin\left(2\pi\left(\frac{x}{\lambda} - ft\right) + \phi\right), \quad (2)$$

where $A_m(x)$ is the amplitude envelope:

$$A_m(x) = A_0 + A_1 x + A_2 x^2.$$

To generalize to a 3D motion, a reciprocal function $z(x,t)$ can be defined with the same structure of (2).
To transform Cartesian coordinates into the curvilinear coordinate $s \in [0, L]$ associated with the backbone, consider the following relation:

$$s(x,t) = \int_0^x \sqrt{1 + \left(\frac{\partial y(u,t)}{\partial u}\right)^2 + \left(\frac{\partial z(u,t)}{\partial u}\right)^2}\, \mathrm{d}u. \quad (3)$$

Applying the inverse of the function (3), a map $x = x(s,t)$ is derived, ensuring that the backbone maintains its length L in compliance with the inextensibility constraint, as explained in [1].
To satisfy the constraint of mass conservation, each segment of the structure needs to be rotated to maintain the same orientation with respect to the backbone. In this project, Euler angles were employed, as illustrated in Figure 4.

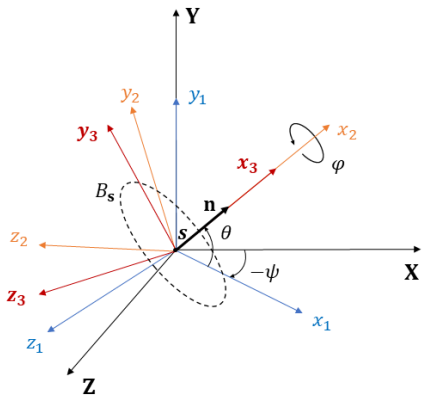

Figure 4: Euler's angles considering the rotation $Y - z_1 - x_2$.

The analytical expressions for the Euler angles are given by:

$$\psi(x,t) = -\arctan\left(\frac{\partial z(x,t)}{\partial x}\right),$$

$$\theta(x,t) = \arctan\left(\frac{\partial y(x,t)/\partial x}{\sqrt{\left(\partial z(x,t)/\partial x\right)^2 + 1}}\right),$$

$$\varphi(x,t) = 2\pi t f_\varphi,$$

where f_φ is the roll frequency.

By constructing the rotation matrix $\mathbf{T}(\mathbf{s},t) = \mathbf{R}_\psi(\mathbf{s},t)\mathbf{R}_\theta(\mathbf{s},t)\mathbf{R}_\varphi(\mathbf{s},t)$, and considering a point $\mathbf{x}^\star$ in the reference configuration, it becomes possible to determine the coordinates $\mathbf{x}$ at time t in the deformed state:

$$\mathbf{x}(\mathbf{x}^*, t) = \mathbf{s} + \mathbf{T}(\mathbf{s},t)(\mathbf{x}^* - \mathbf{s}^*).$$

The visual representation of the strategy is performed in Figure 5.

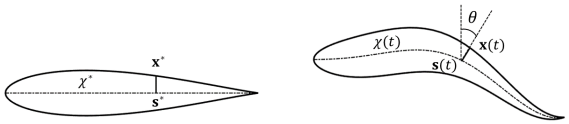

(a) Reference configuration of the structure.

(b) Deformed configuration of the structure at time t.

Figure 5: Illustration of the swimmer surface displacement.

The Lagrangian velocity field of the surface is calculated using second-order backward differencing (BDF2). Additionally, an algorithm has been devised to determine the Eulerian velocity field for solid cells, reconstructing the initial position of the elements and then applying BDF2.

3. Results

To verify the PIMPLE-IBM algorithm, simulations of benchmark cases were performed, including flow over a circular cylinder and undulating motions of a flat plate and NACA0012 airfoil [3]. Subsequently, simulations were conducted to explore both 2D and 3D scenarios of fish-like swimming.

3.1. Two-dimensional simulations

Consider a simulation domain $\Omega = [x_1, x_2] \times [y_1, y_2]$, with an inlet in the left wall, outlet in the right wall and slip condition on the bottom and top, as illustrated in Figure 6.

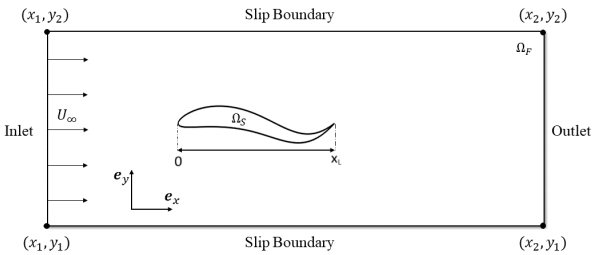

Figure 6: Two-dimensional simulation domain.

In the sensitivity study, a domain $\Omega = [-1, 12] \times [-4, 4]$, a grid size of $h = 2 \times 10^{-2}$ with dynamic local refinement near the fish, and a time step of $\Delta t = 2.5 \times 10^{-3}$ were chosen.
The Reynolds number for aquatic swimming, defined as $Re = {}^{LU_\infty}/_{\nu}$, is set to $Re = 5000$, which is in accordance with previous research on the swimming of the aquatic animal.
The assessment of forces will be conducted utilizing the drag and lift coefficients:

$$C_D = \frac{F_D}{\frac{1}{2}\rho U_\infty^2 L}, \quad C_L = \frac{F_L}{\frac{1}{2}\rho U_\infty^2 L}.$$

The drag force defined in (1) can be decomposed into contributions from the viscous and pressure terms, yielding the pressure drag coefficient C_{DP} and the viscous drag coefficient C_{DF}.
To prescribe the kinematics of the fish in (2), consider the parameter set outlined in Table 1, where T is the transient period.

α	A_0	A_1	A_2	λ	ϕ	T
0.1	0.2	-0.825	1.625	1.0	0.0	0.2

Table 1: Kinematic Parameters.

3.1.1 Frequency analysis

Simulation results for fish-like swimming across frequencies ranging from $f = 0.5$ to 2.0 Hz are presented in Figure 7, showcasing the mean drag coefficients $\overline{C}_D$, $\overline{C}_{DP}$, and $\overline{C}_{DF}$. At high frequencies the drag exhibits a negative value, indicating the presence of a thrust force that drives the propulsion mechanism.

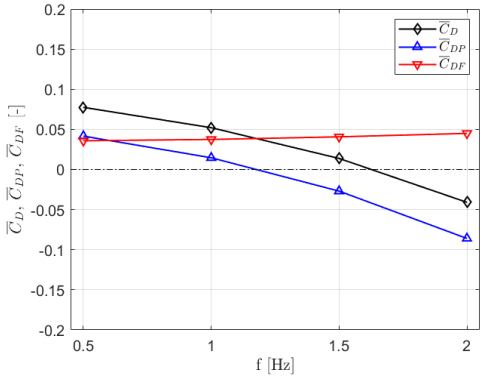

Figure 7: Time average drag coefficients with respect to the frequency.

The vorticity profile defined as $\boldsymbol{\omega} = \nabla \times \mathbf{u}$, was computed for various frequencies and is depicted in Figure 8. The eddies exhibit an alternating direction pattern, and their geometry varies in accordance with the frequency, which modifies the dynamics of the wake.

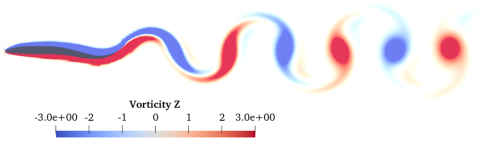

(a) Frequency $f = 1.0$ Hz

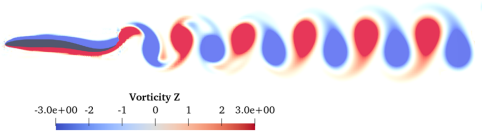

(b) Frequency $f = 2.0$ Hz

Figure 8: Vorticity profile of 2D fish-like swimming.

3.1.2 Amplitude analysis

A study was conducted while maintaining the parameters outlined in Table 1, varying the tail's amplitude α. The resulting curves for the mean drag coefficient $\overline{C}_D$ are illustrated in Figure 9.

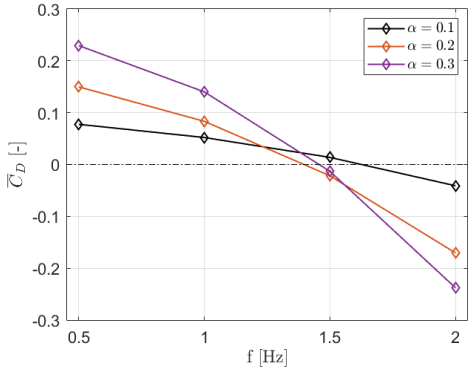

Figure 9: Time average drag coefficient for different amplitudes.

The findings indicate that increasing the amplitude amplifies the drag force's impact, causing higher drag forces at lower frequencies, and adversely affecting swimming. In contrast, at higher frequencies, thrust forces rise, propelling the fish and yielding positive swimming outcomes, which also require more power to generate lateral undulation.

3.1.3 Motion form analysis

To examine the alterations in swimming dynamics, various types of motions were analyzed, specifically comparing the carangiform and anguilliform motions by modifying parameters associated with the amplitude envelope. Illustrated in Figure 10 are the backbone configurations in a cycle of oscillation.

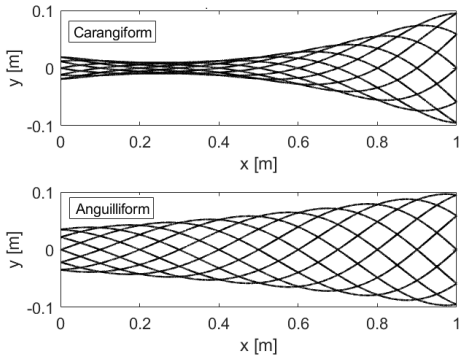

Figure 10: Backbone configuration of the carangiform and anguilliform in a cycle.

The graph portraying the mean drag coefficient against frequency, illustrated in Figure 11, demonstrates that the anguilliform motion exhibits higher drag forces at low frequencies. On the other hand, at higher frequencies, this motion showcases superior propulsion forces.

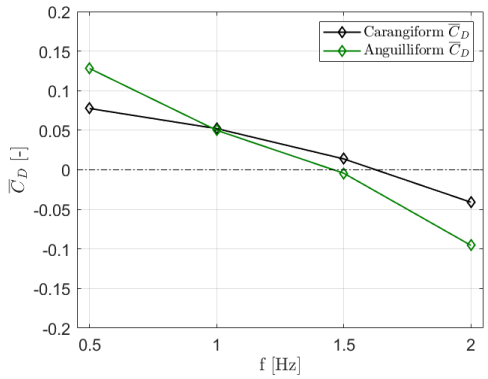

Figure 11: Time average drag coefficient for different motions.

3.2. Three-dimensional simulations

Consider a simulation domain $\Omega = [x_1, x_2] \times [y_1, y_2] \times [z_1, z_2]$, with an inlet in the left wall, outlet in the right wall and slip condition on the bottom, top, front and back, considering regions of local refinement as illustrated in Figure 12.

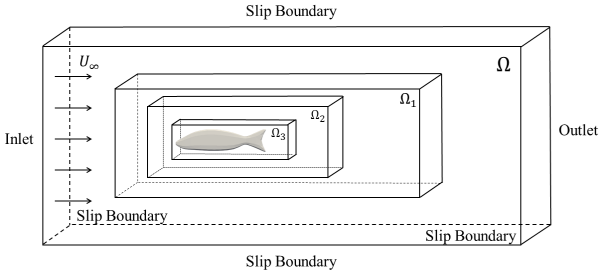

Figure 12: Three-dimensional simulation domain.

A domain $\Omega = [-2, 10] \times [-2, 2] \times [-2, 2]$, a grid size of $h = 5 \times 10^{-2}$ with the local refinement at the wake region, and a time step of $\Delta t = 2.5 \times 10^{-3}$ were chosen. The selected structure resembles a mackerel, representing a realistic fish geometry.
To maintain the swimming profile, conditions of $z(x, t) = 0$ and $f_\varphi = 0$ were imposed, keeping the parameters consistent with Table 1. Simulations were conducted for various oscillation frequencies. The results, obtained using the Q-Criterion method for vortex identification in the flow field, are depicted in Figure 13.

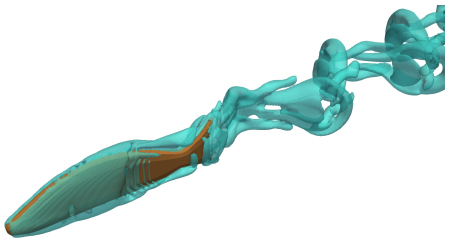

(a) Frequency $f = 1.0$ Hz

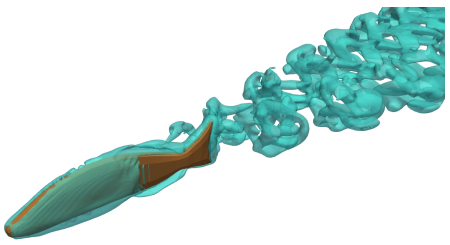

(b) Frequency $f = 2.0$ Hz

Figure 13: Three-dimensional vortical structures using the Q-criterion of $Q = 0.1$.

At lower frequencies, a single trail of eddies appears, oscillating along the fish's central axis. However, at higher frequencies, these eddies split into two distinct lines, expanding sideways. This behavior is linked to the fish's tail exhibiting increased lateral velocity at higher frequencies,

causing the fluid eddies to disperse laterally. These observations align with findings reported in [2].

Figure 14 depicts a horizontal cross-section through the middle of the fish, offering a perspective similar to the 2D simulation previously conducted in Figure 8. The results are aligned, yet a distinction arises in 3D simulations where the lateral dispersion of vortices at a frequency of $f = 2.0$ Hz becomes evident.

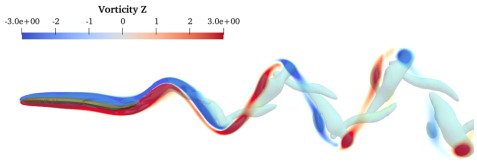

(a) Frequency $f = 1.0$ Hz

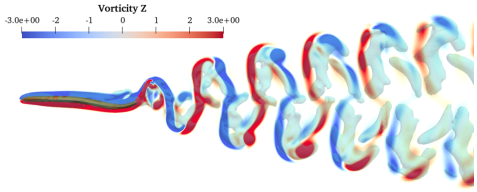

(b) Frequency $f = 2.0$ Hz

Figure 14: Z-plane cross-section vorticity profile in three-dimensional fish-like swimming compared with the Q-criterion profile of $Q = 0.1$.

4. Conclusions

In this study, a kinematic model for fish-like swimming, implemented via the Immersed Boundary method in OpenFOAM, was developed. This model relies on a travelling-wave undulation, supported by a dedicated C++ algorithm designed to maintain inextensibility, mass conservation, and accurately represent the Eulerian velocity field of the solid.

A series of simulations were performed in both two and three dimensions, employing the implemented algorithm for fish-like swimming. This enables the analysis of diverse scenarios encompassing various geometries, frequencies, amplitudes of oscillations, and forms of motion. Through post-processing, comparisons were made between the drag forces and wake vorticity patterns. Then, an analysis was conducted to examine how swimming characteristics influenced the fluid dynamics of the flow and glean insights from these observations.

The results highlight the substantial impact of oscillation frequency on drag force, showcasing an inverse relationship. At higher frequencies, the mean drag coefficient displays negative values, revealing propulsion forces acting within the swim configuration. This analysis was also conducted across various amplitudes and motion types.

Furthermore, the wake's vorticity pattern was found to be responsive to changes in the oscillation frequency. The 3D results highlighted that at lower frequencies, the eddies appeared in a single trail, whereas at higher frequencies, they bifurcated into a double trail pattern.

The limitations of the study consist of an absence of self-propelling swimming modes involving feedback mechanisms for the center of mass movement. Turbulence modelling was omitted, assuming laminar flow. Additionally, 3D simulations were constrained due to project time, limiting the exploration of a broader range of scenarios.

Future efforts should focus on the integration of fluid feedback mechanisms to analyze self-propulsion, delving into parameters such as acceleration, maximum velocity, and swimming efficiency. Moreover, leveraging the developed algorithm opens up the possibility of analyzing a broad spectrum of scenarios encompassing various aquatic animals and motion types.

References

[1] Michel Bergmann and Angelo Iollo. Modeling and simulation of fish-like swimming. *Journal of Computational Physics*, 230(2):329–348, 2011.

[2] Iman Borazjani and Fotis Sotiropoulos. Numerical investigation of the hydrodynamics of carangiform swimming in the transitional and inertial flow regimes. *Journal of experimental biology*, 211(10):1541–1558, 2008.

[3] Gen-Jin Dong and Xi-Yun Lu. Characteristics of flow over traveling wavy foils in a side-by-side arrangement. *Physics of fluids*, 19(5), 2007.

[4] Giorgio Negrini. Non-conforming methods for the simulation of industrial polymer mixing processes. *Ph.D. thesis, Politecnico di Milano*, 2023.